JCB Journal of Cell Biology

**REPORT**

# CAMSAPs organize an acentrosomal microtubule network from basal varicosities in radial glial cells

Laure Coquand[1]*, Guiliana Soraya Victoria[1]*, Alice Tata[1], Jacopo Amerigo Carpentieri[1], Jean-Baptiste Brault[1], Fabien Guimiot[2], Vincent Fraisier[3], and Alexandre D. Baffet[1,4]

**Neurons of the neocortex are generated by stem cells called radial glial cells. These polarized cells extend a short apical process toward the ventricular surface and a long basal fiber that acts as a scaffold for neuronal migration. How the microtubule cytoskeleton is organized in these cells to support long-range transport is unknown. Using subcellular live imaging within brain tissue, we show that microtubules in the apical process uniformly emanate for the pericentrosomal region, while microtubules in the basal fiber display a mixed polarity, reminiscent of the mammalian dendrite. We identify acentrosomal microtubule organizing centers localized in varicosities of the basal fiber. CAMSAP family members accumulate in these varicosities, where they control microtubule growth. Double knockdown of CAMSAP1 and 2 leads to a destabilization of the entire basal process. Finally, using live imaging of human fetal cortex, we reveal that this organization is conserved in basal radial glial cells, a related progenitor cell population associated with human brain size expansion.**

## Introduction

In the developing neocortex, neurons and glial cells are generated by neural stem cells called radial glial (RG) progenitor cells (Kriegstein and Alvarez-Buylla, 2009; Taverna et al., 2014). Two types of closely related RG cells have been identified, with different localization, morphologies, and abundancy. Apical RG (aRG) cells, also known as vRGs, have an epithelial identity and are present in all mammalian species. They are highly elongated bipolar cells, with an apical process attached to the ventricular surface and a basal process (or fiber) extending toward the pial surface of the brain (Fig. 1 A; Paridaen and Huttner, 2014). Basal RG (bRG) cells, also known as oRGs, are rare in lissencephalic (smooth brain) species such as mice and abundant in gyrencephalic (folded brain) species, including humans (Lui et al., 2011; Hansen et al., 2010; Fietz et al., 2010; Reillo et al., 2011). Their relative abundance is believed to account for variations in the size and degree of folding of the neocortex (Fernández et al., 2016). bRG cells derive from aRGs but have delaminated from the neuroepithelium (Fig. 1 A).

The basal process of RG cells has long been known to act as a scaffold, guiding the migration of newborn neurons to their correct position in the neocortex (Noctor et al., 2004; Tan and Shi, 2013). More recently, the basal process has emerged as a potential regulator of cell fate (Shitamukai et al., 2011; Alexandre et al., 2010). Accordingly, a number of molecules important for basal process integrity or for RG cell proliferative capacity have been identified to localize in a polarized manner to the basal process (Yokota et al., 2009, 2010; Tsunekawa et al., 2012). A recent study identified multiple mRNAs associated with Fragile X mental retardation protein that localize to the basal endfeet and travel long distances at velocities consistent with microtubule-based transport (Pilaz et al., 2016).

Organization of the microtubule cytoskeleton is crucial for polarized transport of cargoes to various subcellular locations. Many differentiated cells display an acentrosomal microtubule organization (Bartolini and Gundersen, 2006). In neurons, the axonal microtubule network is unipolar, with the plus ends pointing toward the axonal tip, while in dendrites, microtubules have a mixed polarity (Yau et al., 2016; Baas et al., 1988). This particular microtubule organization depends on γ-tubulin–mediated acentrosomal nucleation, as well as on calmodulin-regulated spectrin-associated family (CAMSAP)/Patronin–mediated minus-end growth (Yau et al., 2014; Feng et al., 2019; Wang et al., 2019).

A variety of genetic mutations have been shown to lead to malformations of cortical development (Pinson et al., 2019). Strikingly, the majority of affected genes code for proteins associated with the microtubule cytoskeleton (Poirier et al., 2013; Jayaraman et al., 2018; Reiner et al., 1993). Few regulators of

---

[1]Institut Curie, Paris Sciences et Lettres Research University, Centre national de la recherche scientifique UMR144, Paris, France; [2]Unité de Fœtopathologie-Université de Paris et Institut national de la santé et de la recherche médicale UMR1141, Hôpital Robert Debré, Paris, France; [3]UMR144-Cell and Tissue Imaging Facility, Centre national de la recherche scientifique–Institut Curie, Paris, France; [4]Institut national de la santé et de la recherche médicale, Paris, France.

*L. Coquand and G.S. Victoria contributed equally to this paper; Correspondence to Alexandre D. Baffet: alexandre.baffet@curie.fr.

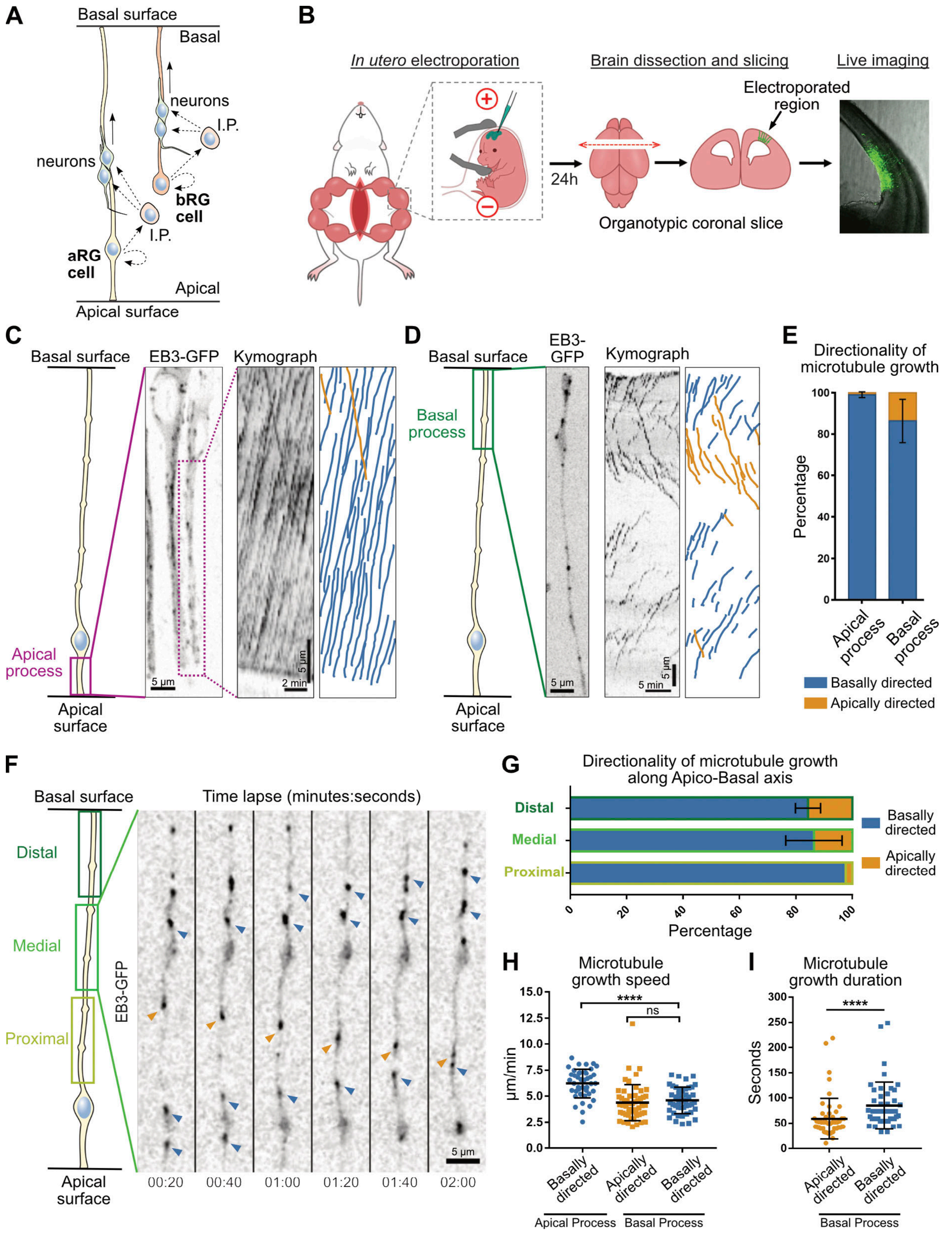

Figure 1. **A bipolar microtubule network in the basal process of aRG cells.** **(A)** Schematic representation of aRG and bRG cells. I.P., intermediate progenitor. **(B)** Experimental setup. **(C)** Left: Live imaging of EB3-GFP in the apical process of mouse aRG cells in situ. Center: Corresponding kymograph. Right: Manual tracks corresponding to the kymograph. **(D)** Left: Live imaging of EB3-GFP in the basal process of mouse aRG cells in situ. Center: Corresponding kymograph. Right: Manual tracks corresponding to the kymograph. **(E)** Quantification of the average directionality of EB3 comets in the apical and basal processes (*n* = 302 comets from 28 cells and 827 comets from 104 cells, respectively). **(F)** Live imaging of EB3-GFP along the apico–basal axis of the basal process of a mouse aRG cell. Blue arrowheads indicate basally growing microtubules, and orange arrowheads indicate apically growing microtubule. **(G)** Quantification of EB3 comet directionality along the proximo–distal axis of the basal process (*n* = 90 comets from 6 cells in apical; 141 comets from 12 cells

in medial; and 198 comets from 12 cells in basal). **(H)** Quantification of the average speed of apically and basally directed EB3 comets in the apical and basal processes (*n* = 40, 52, and 45 comets from 11, 20, and 15 cells, respectively). **(I)** Quantification of the average growth duration of apically and basally directed EB3 comets in the basal process (*n* = 52 and 45 comets from 20 and 15 cells, respectively). Error bars indicate SD. ****, P < 0.0001 by Mann-Whitney tests. All experiments were performed in at least three independent mice.

microtubule organization have been investigated so far in RG cells. The adaptor protein Memo1 controls the localization of CAMSAP2 and the stability and organization of the microtubule network in dissociated mouse RG cell cultures (Nakagawa et al., 2019). In the apical process, the centrosomal protein AKNA promotes microtubule nucleation and regulates aRG cell delamination (Camargo Ortega et al., 2019). The organization and polarity of the microtubule network in aRG and bRG cells in situ is, however, currently unknown. This is largely due to the challenge of studying dynamic subcellular processes in real time within thick organotypic brain cultures.

## Results and discussion

### A bipolar microtubule network in the basal process of aRG cells

To visualize the orientation of growing microtubules in mouse aRG cells in situ, we developed an approach for high-resolution and fast subcellular live imaging within thick embryonic brain slices. GFP-tagged plus-end tracking protein (+TIP) EB3 was delivered to aRG cells using in utero electroporation at embryonic day (E) 13.5 (Baffet et al., 2016). The embryos were then sacrificed 24 h later, and brains were sliced and mounted for imaging using a modified sample preparation and imaging method (see Materials and methods; Fig. 1 B). We first revisited microtubule organization in the apical process of mouse aRG cells (Tsai et al., 2007, 2010). This analysis indicated that over 99% of microtubule plus ends emanated from the apical endfoot, where the centrosome is located, and grew in the basal direction toward the cell soma (Fig. 1, C and E; and Video 1). We then performed a similar analysis in the basal process of aRG cells. In contrast to what we observed in the apical process, growing microtubules adopted a mixed polarity, reminiscent of dendritic microtubule organization (Fig. 1 D and Video 2). This organization, however, remained biased toward basally directed growth, as only 15% of microtubules grew in the apical direction (Fig. 1 E). Most EB3 comets did not grow from the apical centrosome but directly emanated from the basal process. Bipolar microtubule organization was observed in the distal and medial parts of the basal process, but not in the proximal part where the network was largely unipolar, likely due to the proximity of the centrosome (Fig. 1, F and G; and Video 3). Apically and basally directed microtubules within the basal fiber grew at similar speeds, but slower than in the apical process (Fig. 1 H). Finally, in the basal process, basally directed microtubules grew for longer durations than apically directed ones, suggesting higher stability (Fig. 1 I). Therefore, microtubules in the apical process of aRG cells emanate from the pericentrosomal region and form a unipolar network growing in the basal direction, while microtubules in the basal process appear largely acentrosomal and have a bipolar orientation biased toward basal growth.

### *Acentrosomal microtubules preferentially grow from varicosities of the basal process*

We next asked whether acentrosomal microtubule organizing centers may exist within the basal process of aRG cells. From the observation of the EB3-GFP movies, we noted that a large number of newly appearing comets emanated from varicosities of the basal process (Fig. 1 D). Varicosities (also known as swellings) are well known but poorly described deformations of RG cell basal processes, with no reported function (Noctor et al., 2001; Hansen et al., 2010; Hu et al., 2013). We could observe these structures following expression of soluble GFP or immunostaining against the RG-specific protein Nestin (Fig. 2, A and B). Long-term imaging of varicosities revealed that they remained largely stable over the course of 22-h movies (Fig. 2 C, Video 4, and Video 5).

To measure microtubule growth from these structures, we live imaged a large number of varicosities as well as basal process shafts (nondeformed regions) in EB3-GFP–expressing cells and quantified the rate of new EB3 comet formation in these two domains. This analysis revealed that the average rate of comet formation in varicosities was 11.4 times higher than in the rest of the shaft (Fig. 2, D and E; and Video 6). Moreover, while 89.6% of comets emanating from the shaft grew in the basal direction, microtubules emanating from varicosities appeared initially more bipolar, albeit still with a basal bias (65.7%; Fig. 2 F). This analysis therefore identifies varicosities of the basal process of mouse aRG cells as acentrosomal microtubule organizing centers.

### *Dendrite-like microtubule organization from varicosities is a conserved feature of human bRG cells*

Because bRG cells share many characteristics with aRG cells, we next asked if bipolar microtubule organization from basal process varicosities was also a feature of these cells. To test this, we developed a protocol to electroporate and live image pieces of human fetal frontal cortex biopsies obtained from second-trimester medical pregnancy terminations (Fig. 3, A and B; and see Materials and methods). We identified bRG cells based on their localization in the subventricular zone and their morphology. These cells were further positive for the RG marker Sox2 and performed mitotic somal translocation (MST; Fig. S1, A and B; and Video 7). We first confirmed the presence of numerous varicosities all along the basal process of human bRG cells, which were visible following GFP electroporation or immunostaining against Vimentin (Fig. 3, C and D). We next expressed EB3-GFP in human fetal cortex samples and recorded plus-end microtubule growth in bRG cell varicosities. Similar to our observations in mouse aRG cells, we observed abundant de novo EB3 comet formation within varicosities (Fig. 3 E and Video 8). As in aRG cells, the rate of EB3 comet formation inside varicosities was much

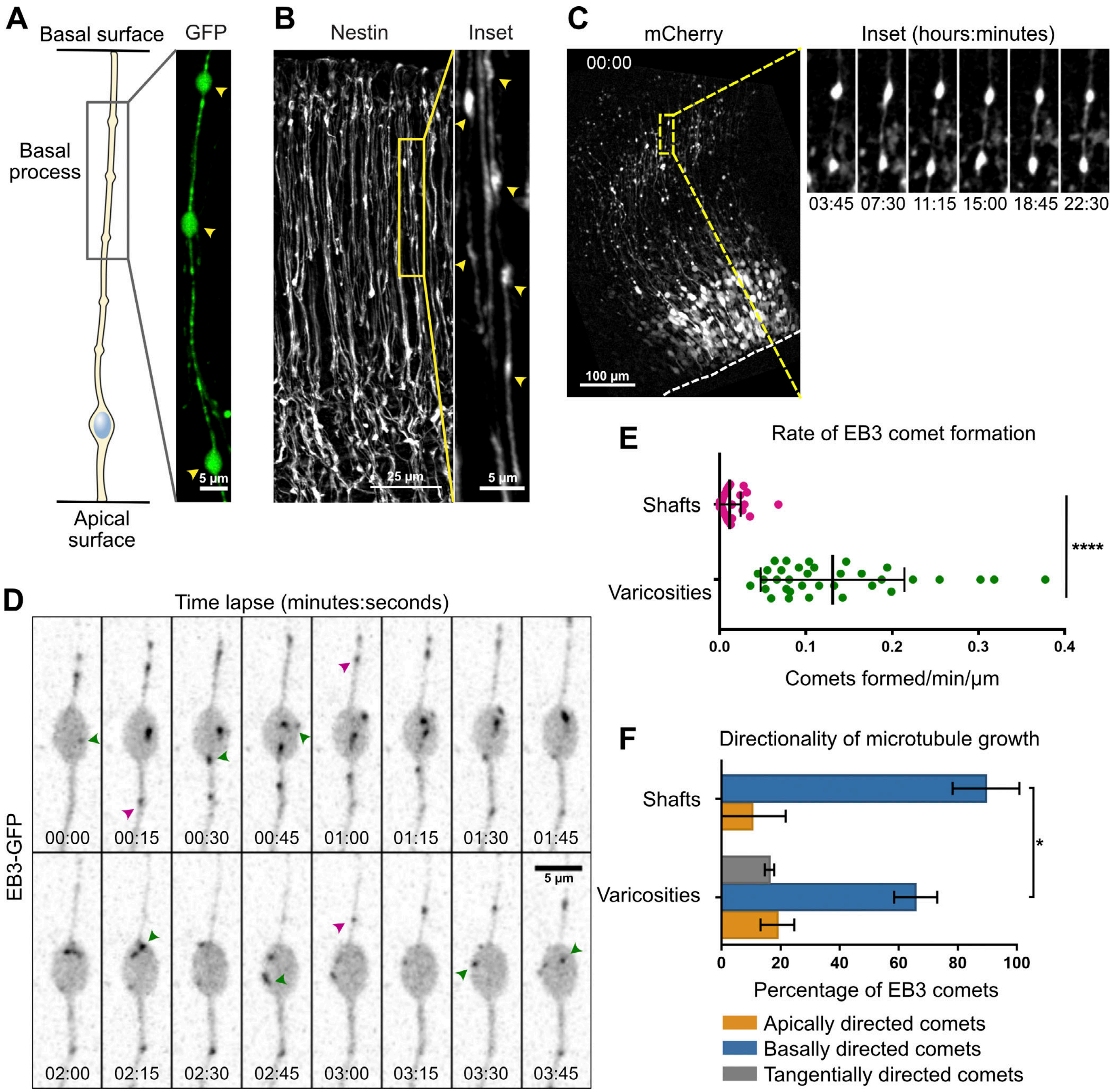

Figure 2. **Acentrosomal microtubules preferentially grow from varicosities of the basal process. (A and B)** The basal processes of aRG cells display varicosities (arrowheads), visualized by overexpression of GFP (A) and immunofluorescence against Nestin (B). **(C)** Live imaging of mCherry-expressing mouse aRG cells reveals stable varicosities over the course of a 24-h movie. Dashed line marks apical surface. **(D)** Live imaging of EB3-GFP in the basal process of an aRG cell showing the emergence of new comets within a varicosity. Green arrowheads: newborn comets in the varicosity. Purple arrowheads: newborn comets in the shaft. **(E)** Quantification of the rate of EB3 comet formation in basal process shafts and varicosities, normalized to length ($n$ = 40 shafts and 34 varicosities from 39 cells). **(F)** Quantification of the average directionality of EB3 comets in the shafts and varicosities of the basal processes ($n$ = 122 comets from 62 shafts and 260 comets from 65 varicosities). **(E and F)** Error bars indicate SD. *, $P < 0.05$; ****, $P < 0.0001$ by Mann-Whitney tests. All experiments were performed in at least three independent mice.

stronger than in the rest of the shaft (Fig. 3 F). We next analyzed the directionality of EB3 comets in the basal process of human bRG cells, which revealed, as for mouse aRG cells, a bipolar microtubule network biased toward basal growth (82.3 ± 84.5%; Fig. 3 G). Finally, we compared the size of varicosities in mouse aRG and human fetal bRG cells. This analysis revealed relatively variable size, but on average was similar between the two cell types (Fig. 3 H). While the distance between two consecutive varicosities was quite variable, their frequency was substantially higher in human bRG cells than in mouse aRG cells (Fig. 3 I). Therefore, bipolar microtubule network organization from basal process

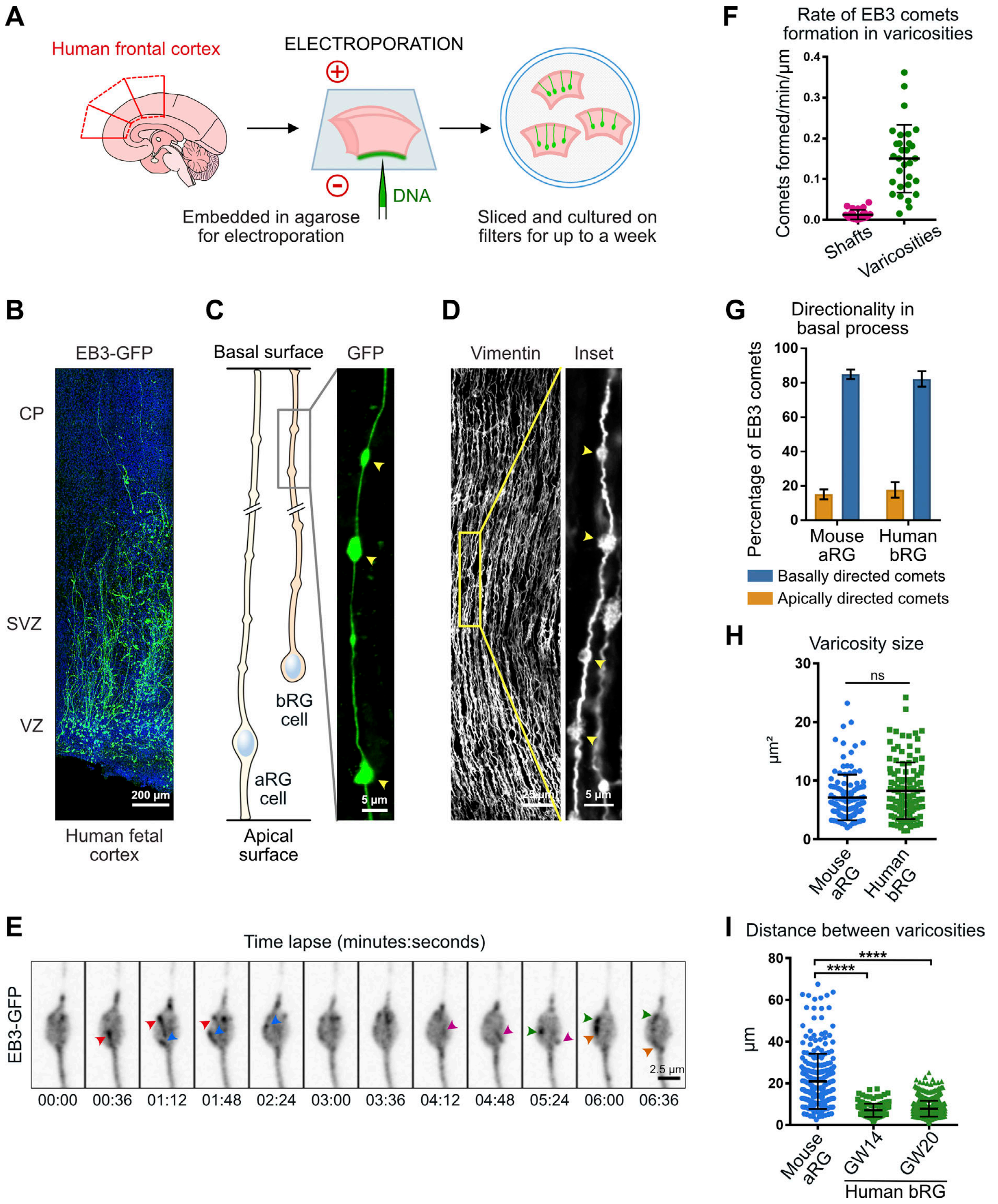

Figure 3. **Dendritic-like microtubule organization from varicosities is a conserved feature of human bRG cells. (A)** Schematic of protocol as described in Materials and methods. **(B)** A slice of human fetal cortex electroporated with EB3-GFP. CP, cortical plate; SVZ, subventricular zone; VZ, ventricular zone. **(C and D)** The basal processes of human bRG cells display varicosities, visualized by overexpression of GFP (C) and immunofluorescence against Vimentin (D). **(E)** Live imaging of a human bRG cell showing appearance of de novo EB3 comets (arrowheads) in a basal process varicosity. **(F)** Quantification of the rate of EB3 comet formation in basal process shafts and varicosities of human bRG cells at gestational week (GW) 18 (*n* = 24 shafts and 30 varicosities from 20 cells). **(G)** Quantification of the overall directionality of EB3 comets in the basal process of human bRG cells (*n* = 205 comets from 7 cells). Mouse data from Fig. 1 F are shown for comparison. **(H)** Quantification of varicosity size in mouse (E14.5) and human (GW 14 and 20) tissue (*n* = 55, 129, and 772 varicosities from 11, 36, and 82 cells, respectively). **(I)** Quantification of the distance between individual varicosities along the basal process in mouse (E14.5) and human (GW 14 and 20) tissue (*n* = 260 and 605 varicosities from 36 and 82 cells, respectively). Error bars indicate SD. ****, P < 0.0001 by Mann-Whitney tests. Experiments were performed in two independent human fetal brains and three independent mice.

varicosities appears to be conserved between mouse aRG and human bRG neural stem cells.

### CAMSAPs localize to varicosities and are required for microtubule growth

We next investigated the localization of the key microtubule nucleator, the γ-tubulin ring complex. Expression of mEmerald–γ-Tubulin revealed its expected enrichment in the pericentrosomal region at the base of the apical process (Fig. 4 A). However, γ-tubulin was undetectable within the basal process, both in varicosities and in the rest of the shaft (Fig. 4 A). We next tested whether growing microtubules preferentially emerged from basal process varicosities due to an accumulation of stabilized microtubule minus ends within these structures. Members of the CAMSAP family (CAMSAP1, 2, and 3) specifically recognize and stabilize microtubule minus ends, generating seeds from which multiple rounds of plus-end growth and shrinkage can occur (Jiang et al., 2014). GFP-tagged CAMSAP1, 2, and 3 accumulated at the ventricular surface but also strongly accumulated within varicosities (Fig. 4, B–D). CAMSAP1 was particularly abundant at the edges of the varicosities, where microtubules are often observed to emanate (Fig. 4 C). CAMSAPs could also occasionally be observed in the shafts, where EB3 comet formation is lower. Moreover, CAMSAP clusters were much larger within varicosities than in the shaft (Fig. 4 F). Immunostaining for CAMSAP1, 2, and 3 revealed a punctuated signal within mouse and human RG cell varicosities in vivo, as well as in the processes of human RG cells cultured in vitro (Fig. S2, A–C).

We then live imaged GFP-tagged CAMSAP1, 2, and 3 together with EB3-mCherry within mouse embryonic brain slices. While GFP–CAMSAP1 and 2 low expression levels only allowed us to perform movies in very few cells, imaging of CAMSAP3-GFP confirmed a strong association between CAMSAP3 and comet formation hotspots (Fig. 4, F and G; Video 9 and Video 10). Quantification revealed that the majority of newly formed EB3-mCherry comets were observed emanating from CAMSAP3-GFP clusters, especially within varicosities (Fig. 4 H). EB3 comets emanating within or away from CAMSAP3$^+$ foci had the same polarity, and expression of CAMSAP3-GFP did not affect EB3 comet rates (Fig. S2 D and not shown).

Transcriptomic data indicate that CAMSAP1 and 2 are expressed at higher levels than CAMSAP3 in mouse aRG cells, and we therefore focused on these two factors (Telley et al., 2019). shRNA-mediated knockdown (KD) of CAMSAP1 and 2 led to a rapid destabilization of the entire basal process of aRG cells, indicating a critical function for basal process architecture (Fig. 5 A). Single KD of CAMSAP1 mildly altered basal process integrity, while CAMSAP2 KD had no clear effect. We therefore analyzed the rate of EB3 comet formation in CAMSAP1 and CAMSAP2 KD varicosities, which revealed 38% and 52% reductions, respectively (Fig. 5, B and C; Video 11, Video 12, and Video 13). EB3 comet formation within shafts was not significantly affected, suggesting that these comets correspond to rescue events (Fig. 5 D). Overall, these results indicate that microtubules preferentially grow from varicosities of the basal process in a CAMSAP 1 and 2–dependent manner.

### A TGN-related compartment localizes to microtubule minus ends in basal process varicosities

Because the Golgi apparatus is a major site for acentrosomal microtubule organization, we next asked whether Golgi outposts could be found along the basal process of aRG cells, similar to what happens in dendrites (Horton and Ehlers, 2003; Horton et al., 2005; Ye et al., 2007). In the apical process, where the Golgi apparatus is localized, we consistently detected the cis-medial marker ManII and the trans marker GalNAcT2, as well as the small GTPase Rab6A (Fig. S3 A). Strikingly, the trans and TGN markers Rab6A, GalNAcT2, GalT, and TGN46 also localized within the basal process and accumulated within the vast majority of varicosities (87.8 ± 5.1% for GalNAcT2; Fig. S3, B and C). GalNaT2 foci could also be observed by immunostaining (Fig. S3, D and E). The cis-medial markers ManII and GMAP210 were, however, undetectable outside the apical process (381 varicosities out of 36 cells and 235 varicosities out of 27 cells were analyzed, respectively; Fig. S3 B). These results point toward the presence of a Golgi-related secretory compartment with a trans-Golgi/TGN identity in basal process varicosities of RG cells.

Consistent with CAMSAP2 recruitment to the cis-Golgi (Wu et al., 2016), CAMSAP3 did not colocalize with the trans marker GalNacT2 in basal process varicosities. However, we noted that CAMSAP3 and GalNacT2 were frequently found in close proximity (Fig. S3 F). Because the trans-Golgi and TGN can stimulate microtubule growth via the recruitment of CLASP 1 and 2 (Efimov et al., 2007), we asked whether microtubules preferentially grew from GalNacT2-positive foci. This analysis revealed an association between GalNacT2-positive structures and newly formed EB3 comets (72 ± 6.8%), which was stronger in varicosities (81.3 ± 5.1%) than in shafts (42.9 ± 21.25%; Fig. S3, G and H; and Video 14). EB3 comets emanating outside or within GalNacT2$^+$ foci had a similar polarity (Fig. S3 I). These results suggest a role for Golgi membranes in the growth of minus end–stabilized microtubules within varicosities of RG cell basal processes. The presence of trans and TGN markers, but not cis-medial elements, argues against the presence of canonical Golgi outposts and rather points to a secretory structure, presumably with a TGN identity. Our observations are consistent with an electron microscopy study revealing a lack of Golgi cisternae in the basal process of aRG cells (Taverna et al., 2016).

### A dendrite-like microtubule network is organized from basal fiber varicosities

The basal process organization is reminiscent of what has been described in the mammalian dendrite, where one third of dynamic microtubules are “minus end out,” growing toward the soma (Baas et al., 1988; Baas and Lin, 2011). This polarity suggests that trafficking into the basal process is likely to rely on kinesin-based movement but that minus end–based transport of specific cargos—as shown in dendrites (Kapitein et al., 2010)—cannot be ruled out. It is important to stress that EB3 tracking specifically probes the polarity of dynamic microtubules, and is only an approximation for the overall microtubule polarity. Indeed, laser-cut and motor-PAINT experiments performed in hippocampal neurons in culture have revealed an even greater proportion of minus end out microtubules (Yau

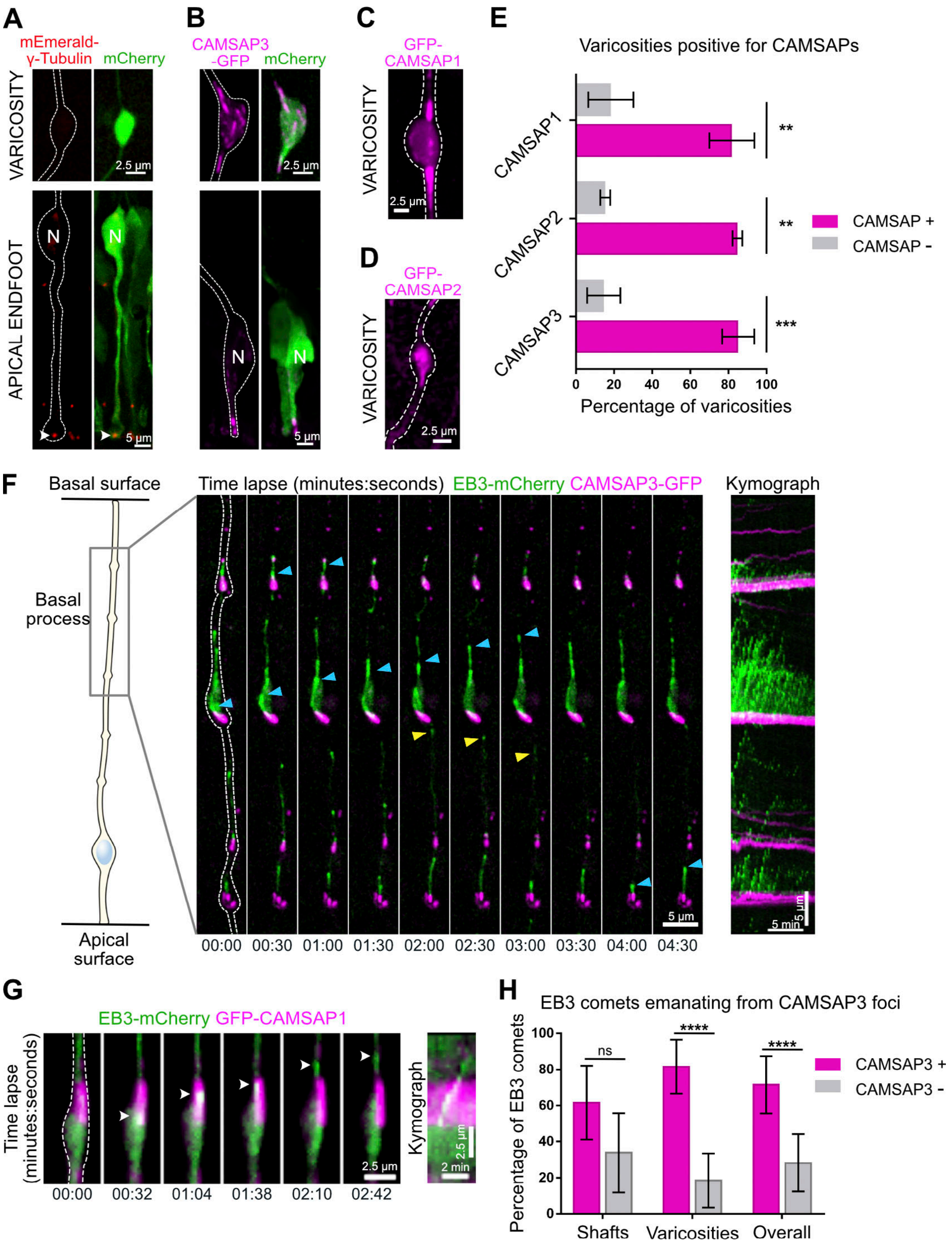

Figure 4. **Basal process microtubules grow from CAMSAP-positive foci. (A and B)** mEmerald–γ-Tubulin and CAMSAP3-GFP localization in mouse aRG cell apical endfeet and basal process varicosities. N, nucleus. **(C and D)** GFP-CAMSAP1 and GFP-CAMSAP2 localization in mouse aRG cell basal process varicosities. CAMSAP1 concentrates on the edges of the swellings. **(E)** Quantification of the percentage of basal process varicosities positive for CAMSAP1, 2, and 3 (*n* = 88 varicosities from 65 cells, *n* = 35 varicosities from 20 cells, and *n* = 120 varicosities from 59 cells, respectively). **(F)** Live imaging of CAMSAP3-GFP and EB3-mCherry in mouse aRG cell basal process and corresponding kymograph. Blue arrowheads: basally growing microtubules. Yellow arrowhead: apically growing microtubules. **(G)** Live imaging of GFP-CAMSAP1 and EB3-mCherry in mouse aRG cell basal process and corresponding kymograph. White arrowhead: EB3 comet emanating from CAMSAP1 foci. **(H)** Quantification of the percentage of EB3 comets emanating from CAMSAP3-positive foci throughout the basal process, in shafts and in varicosities (*n* = 310 comets from 15 cells). **, $P < 0.01$; ***, $P < 0.001$; ****, $P < 0.0001$ by Mann-Whitney tests. All experiments were performed in at least three independent mice. Error bars indicate SD.

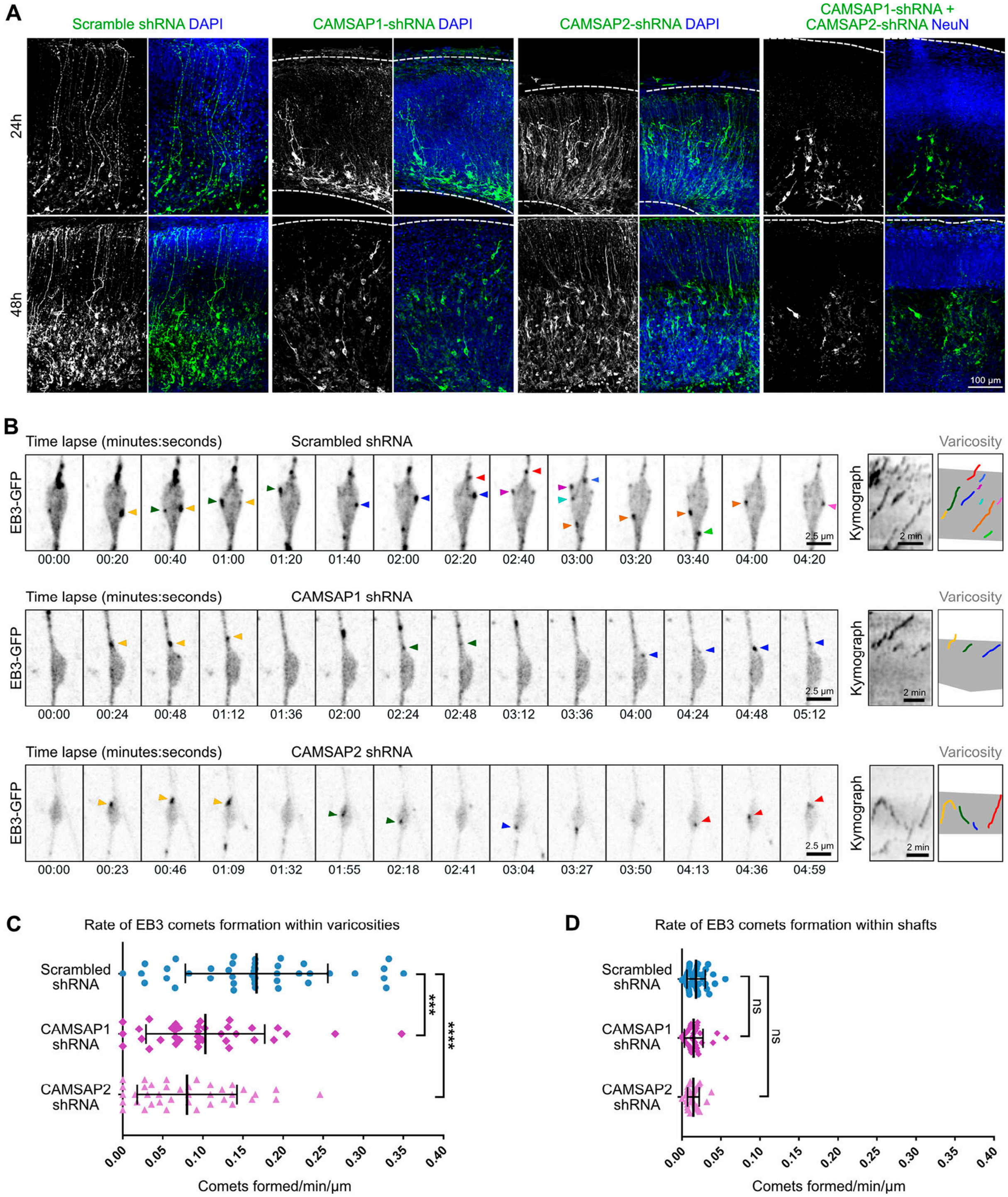

Figure 5. **CAMSAP1 and 2 KD alters microtubule growth from varicosities and basal process architecture. (A)** KD of CAMSAP1 and 2 destabilizes the basal process. E14.5 embryos were in utero electroporated with shRNA-expressing plasmids or scramble control and fixed at E15.5 and E16.5. Brains were stained for DAPI or NeuN to visualize basal surface. Dashed lines indicate apical (bottom) and basal (top) surfaces. **(B)** Live imaging of EB3-GFP in varicosities of RG cells expressing CAMSAP1 shRNA, CAMSAP2 shRNA, or scramble control. Right: Kymographs highlighting reduced EB3 comet formation in CAMSAP1 and 2 KD. Arrowheads: newly formed EB3 comets. **(C)** Quantification of the rate of EB3 comet formation within varicosities of scramble shRNA (*n* = 42 varicosities), CAMSAP1 shRNA (*n* = 35 varicosities), and CAMSAP2 shRNA (*n* = 38 varicosities). **(D)** Quantification of the rate of EB3 comet formation within shafts of scramble shRNA (*n* = 41 varicosities), CAMSAP1 shRNA (*n* = 35 varicosities), and CAMSAP2 shRNA (*n* = 38 varicosities). ***, P < 0.001; ****, P < 0.0001 by Mann-Whitney tests. All experiments were performed in nine brains from three independent mice.

et al., 2016; Tas et al., 2017). The identification of microtubule organizing centers throughout the basal process is consistent with microtubules growing both apically and basally, but how the polarity of the network is biased toward basal growth remains unclear. In axons, unipolar microtubule organization depends on the HAUS/augmin complex (Cunha-Ferreira et al., 2018; Sánchez-Huertas et al., 2016). This complex was recently shown to be critical for γ-tubulin–mediated nucleation from presynaptic boutons (Qu et al., 2019), where increased microtubule dynamics favors delivery of synaptic vesicle precursors (Guedes-Dias et al., 2019).

Based on the absence of γ-tubulin, varicosities do not appear to be sites of microtubule nucleation (Ori-McKenney et al., 2012), but rather sites of minus-end stabilization. Although we cannot rule out the presence of undetectable amounts of γ-tubulin in varicosities, the localization of the minus-end capping proteins CAMSAP1, 2, and 3 further supports this notion. If microtubules are not nucleated within the basal process, where could stabilized seeds come from? One possibility is that acentrosomal microtubules are generated in the apical process by severing enzymes such as spastin or katanin. Alternatively, such severing could occur directly within the basal process in order to amplify the number of acentrosomal microtubules. Interestingly, human mutations in *KATNB1*, which encodes the p80 subunit of katanin, cause severe microcephaly and lissencephaly (Hu et al., 2014). While mitotic and ciliary defects were reported in mutant RG cells, the role of katanin in interphasic microtubule organization was not addressed. Together, this work identifies the organization of the microtubule cytoskeleton in mouse and human RG cells, and will allow to determine how genetic mutations targeting microtubule regulators may affect these neural progenitor cells, leading to brain malformations.

## Materials and methods

### Ethics statement

For animal care, we followed the European and French National Regulation for the Protection of Vertebrate Animals used for Experimental and other Scientific Purposes (Directive 2010/63; French Decree 2013-118). The project was authorized by and benefited from guidance of the Animal Welfare Body, Research Centre, Institut Curie. CD1-IGS pregnant females were purchased from Charles River Laboratories.

Human fetal tissue samples were collected with previous patient consent and in strict observance of legal and institutional ethical regulations. The protocol was approved by the French biomedical agency (Agence de la Biomédecine; approval no. PFS17-003).

### In utero electroporation of mouse embryonic cortex

Pregnant CD1-IGS mice at E13.5 were anesthetized with isoflurane gas and injected subcutaneously first with buprenorphine (0.075 mg/kg) and a local analgesic, bupivacaine (2 mg/kg), at the site of the incision. Lacrinorm gel was applied to the eyes to prevent dryness/irritation during the surgery. The abdomen was shaved and disinfected with ethanol and antibiotic swabs and then opened, and the uterine horns were exposed. Plasmid DNA mixtures were used at a final concentration of 1 µg/µl per plasmid, dyed with Fast Green, and injected into the left lateral ventricle of several embryos. The embryos were then electroporated through the uterine walls with a NEPA21 Electroporator (Nepagene) and a platinum-plated electrode (five pulses of 50 V for 50 ms at 1-s intervals). The uterus was replaced, and the abdomen was sutured. The mother was allowed to recover from surgery and supplied with painkillers in drinking water after surgery.

### Electroporation of human fetal cortex

Fresh tissue from human fetal cortex was obtained from autopsies. A piece of prefrontal cortex was collected from one hemisphere and transported on ice to the laboratory. The tissue was divided into smaller pieces, and embedded 4% low-gelling agarose (Sigma) was dissolved in artificial cerebrospinal fluid (ACSF). Plasmid DNA (1 µg/µl) was injected with a fine glass micropipette through the agarose at the ventricular surface. The gel block was then subjected to a series of five pulses of 50 V for 50 ms at 1-s intervals and sliced with a Leica VT1200S vibratome (300-µm-thick slices) in ice-cold ACSF. Slices were grown on Millicell culture inserts (Merck) in cortical culture medium (DMEM-F12 containing B27, N2, 10 ng/ml FGF, 10 ng/ml EGF, 5% fetal bovine serum, and 5% horse serum) for up to 5 d. Medium was changed every day.

### Subcellular live imaging in mouse embryonic brain and human fetal cortex slices

To record EB3-GFP or EB3-mCherry dynamics together with Golgi markers or CAMSAP3-GFP in radial glia in situ, we used the following approach. 24 h after the electroporation, the pregnant mouse was sacrificed and the electroporated embryos were recovered. Brains were dissected in ACSF, and 300-µm-thick coronal slices were prepared with a Leica VT1200S vibratome in ice-cold ACSF. The slices were cultured on membrane filters over enriched medium (DMEM-F12 containing B27, N2, 10 ng/ml FGF, 10 ng/ml EGF, 5% fetal bovine serum, and 5% horse serum). After recovery in an incubator at 37°C, 5% $CO_2$ for 2 h (or 48 h for human tissue to allow for construct expression), the filters were cut and carefully turned over on a 35-mm FluoroDish (WPI) in order to position the sample in direct contact with the glass, underneath the filter (which maintained the sample flat). Live imaging was performed on a spinning-disk wide microscope equipped with a Yokogawa CSU-W1 scanner unit to increase the field of view and improve the resolution deep in the sample. The microscope was equipped with a high working distance (0.3 mm) 100× SR HP Plan Apo 1.35 NA Silicon immersion (Nikon) or a 60× 1.27 NA Apo plan objective (Nikon) and a Prime95B sCMOS camera. Z-stacks of 15–20-µm range were taken with an interval of 1 µm, and maximum projections were performed from which kymographs were generated. Quantification of EB3 comets frequency and directionality was directly performed on the movies, and the kymographs were used for validation and display purposes. Videos were mounted in Metamorph. Image analysis (kymographs and other quantifications) and modifications of brightness and contrast were performed on Fiji. Figures were assembled in Affinity Designer.

### Immunostaining of brain slices

Mouse embryonic brains were dissected out of the skull and fixed in 4% PFA for 2 h, and 80-µm-thick slices were prepared with a Leica VT1200S vibratome in PBS. Human fetal slices in culture were fixed in 4% PFA for 2 h. Slices were boiled in citrate sodium buffer (10 mM, pH 6) for 20 min and cooled down at room temperature (antigen retrieval). Slices were then blocked in PBS–Triton X-100 0.3%–Donkey serum 2% at room temperature for 2 h, incubated with primary antibody overnight at 4°C in blocking solution, washed in PBS-Tween 0.05%, and incubated with secondary antibody overnight at 4°C in blocking solution before final wash and mounting in aquapolymount. Mosaics (tilescans) of fixed human tissue were acquired with a 40× Apo-Plan objective.

### Expression constructs and antibodies

The following plasmids were used in this study: GFP-CAMSAP1 and GFP-CAMSAP2 (a gift from Anna Akhmanova); CAMSAP3-GFP (a gift from Masatoshi Takeichi); EB3-GFP (a gift from Matthieu Piel); EB3-mCherry (Michael Davidson; Addgene 55037); mCherry2-C1 empty vector (Michael Davidson; Addgene 54563); mEGFP-C1 empty vector (Michael Davidson; Addgene 54759); mEmerald–γ-Tubulin (Michael Davidson; Addgene 54105); GFP-Rab6A (a gift from Bruno Goud); GFP-GMAP210 (a gift from Claire Hivroz); and GalT-mCherry, GalNacT2-mCherry, ManII-GFP, and TGN46-GFP (all gifts from Franck Perez). Antibodies used in this study were mouse anti-Nestin (BD PharMingen; 556309; 1/500), rabbit-anti GalNacT2 (Abcam; AB102650; 1/100), rabbit anti-CAMSAP1 (Novus; NBP1 26645; 1/500), rabbit anti-CAMSAP2 (Novus; NBP1 21402; 1/500), mouse anti-CAMSAP3 (Sigma; SAB4200415; 1/500), mouse anti-SOX2 (Abcam; Ab79351; 1/500), and rat anti-Vimentin (R&D Systems; MAB2105; 1/500).

### Real-time RT-PCR

Neuro2A cells were transfected with CAMSAP1, CAMSAP2, and scramble control shRNA plasmids using Lipofectamin-3000 (Thermo Fisher Scientific). After 3 d, cells were lysed in TRIZOL (Thermo Fisher Scientific). mRNAs were isolated as follows: TRIZOL + sample solution was exposed to chloroform for 7 min at room temperature and centrifuged at 15,000 *g* for 30 min at 4°C. The translucent solution formed was then transferred in 1 ml isopropanol, incubated 7 min at room temperature, and centrifuged at 4°C at 10,000 *g*. The pellet of nucleic acid formed was then washed in ethanol 70% and centrifuged 5 min at 10,000 *g* at 4°C. The pellet was then resuspended in water. The nucleic acid solution was purified from DNA using TURBO DNA-free Kit (Thermo Fisher Scientific). The mRNA obtained was then retrotranscribed using the RT Reverse Transcription Kit (Thermo Fisher Scientific). Real-time RT-PCR was performed using the qPCR Master Mix kit (Thermo Fisher Scientific) and the CAMSAP1 and 2 forward/reverse primers; GAPDH was used for internal control and for normalization. Primers used for CAMSAP1 are forward: 5′-CTTCCTCTTTGGCCTCTGTG-3′, reverse: 5′-AGTGTGGGTTGGTAGCAGT-3′. Primers used for CAMSAP2 are forward: 5′-ATCTCCCAAAACACCGATCA-3′, reverse: 5′-AAGTTGTGGAGCGTTTTCC-3′.

### Online supplemental material

Fig. S1 shows the method of identification of bRG cells in human fetal tissue. Fig. S2 depicts the endogenous distribution of CAMSAP1, 2, and 3, as well as KD efficiency. Fig. S3 illustrates localization of a TGN-related compartment in varicosities of the basal process. Video 1 shows EB3-GFP dynamics in apical process of mouse aRG cells. Video 2 shows EB3-GFP dynamics in the basal process of mouse aRG cells. Video 3 shows EB3-GFP dynamics in the medial part of the basal process of mouse aRG cells. Video 4 shows long-term dynamics of basal process swelling. Video 5 shows long-term dynamics of basal process swelling (inset). Video 6 shows EB3-GFP dynamics in basal process swelling of mouse aRG cells. Video 7 shows a human bRG cell undergoing MST. Video 8 shows EB3-GFP dynamics in basal process swelling of human bRG cells. Video 9 shows EB3-mCherry comets emanating from CAMSAP3-GFP foci. Video 10 shows EB3-mCherry comets emanating from GFP-CAMSAP1 foci. Video 11 shows EB3-GFP dynamics in a varicosity of a scramble shRNA-expressing RG cell. Video 12 shows EB3-GFP dynamics in a varicosity of a CAMSAP1 shRNA-expressing RG cell. Video 13 shows EB3-GFP dynamics in a varicosity of a CAMSAP2 shRNA-expressing RG cell. Video 14 shows EB3-GFP comets emanating from GalNacT2-RFP foci.

## Acknowledgments

We acknowledge the Cell and Tissue Imaging facility of Institut Curie. We thank Franck Perez (Institut Curie, Paris, France), Matthieu Piel (Institut Curie, Paris, France), Claire Hivroz (Institut Curie, Paris, France), Bruno Goud (Institut Curie, Paris, France), Anna Akhmanova (Utrecht University, Utrecht, Netherlands), Michael Davidson (Florida State University, Tallahassee, FL) and Masatoshi Takeichi (RIKEN, Kobe, Japan) for reagents and advice. We thank Renata Basto, Franck Perez, and Bruno Goud for helpful discussions and critical reading of the manuscript.

L. Coquand was funded by a Paris Sciences et Lettres/Sorbonne Université fellowship, G.S. Victoria by Institut Curie and the Ville de Paris, and J.B. Brault by Paris Sciences et Lettres and the Ville de Paris. A.D. Baffet is an Institut national de la santé et de la recherche médicale researcher. This work was supported by the Centre National de la Recherche Scientifique, Institut Curie, the Ville de Paris "Emergences" program, Labex CelTisPhyBio (11-LBX-0038), and Paris Sciences et Lettres.

The authors declare no competing financial interests.

Author contributions: L. Coquand, G.S. Victoria, and A.D. Baffet conceived the project, analyzed the data, and wrote the manuscript. L. Coquand and G.S. Victoria did most of the experimental procedures. A. Tata performed varicosity characterization experiments. J.A. Carpentieri performed RT-quantitative PCR. J.B. Brault and V. Fraisier contributed with high-resolution microscopy in the brain. F. Guimiot provided human fetal samples. A.D. Baffet supervised the project.

Submitted: 25 March 2020
Revised: 30 November 2020
Accepted: 29 April 2021

## References

Alexandre, P., A.M. Reugels, D. Barker, E. Blanc, and J.D.W. Clarke. 2010. Neurons derive from the more apical daughter in asymmetric divisions in the zebrafish neural tube. *Nat. Neurosci.* 13:673–679. https://doi.org/10.1038/nn.2547

Baas, P.W., and S. Lin. 2011. Hooks and comets: The story of microtubule polarity orientation in the neuron. *Dev. Neurobiol.* 71:403–418. https://doi.org/10.1002/dneu.20818

Baas, P.W., J.S. Deitch, M.M. Black, and G.A. Banker. 1988. Polarity orientation of microtubules in hippocampal neurons: uniformity in the axon and nonuniformity in the dendrite. *Proc. Natl. Acad. Sci. USA.* 85: 8335–8339. https://doi.org/10.1073/pnas.85.21.8335

Baffet, A.D., A. Carabalona, T.J. Dantas, D.D. Doobin, D.J. Hu, and R.B. Vallee. 2016. Cellular and subcellular imaging of motor protein-based behavior in embryonic rat brain. *Methods Cell Biol.* 131:349–363. https://doi.org/10.1016/bs.mcb.2015.06.013

Bartolini, F., and G.G. Gundersen. 2006. Generation of noncentrosomal microtubule arrays. *J. Cell Sci.* 119:4155–4163. https://doi.org/10.1242/jcs.03227

Camargo Ortega, G., S. Falk, P.A. Johansson, E. Peyre, L. Broix, S.K. Sahu, W. Hirst, T. Schlichthaerle, C. De Juan Romero, K. Draganova, et al. 2019. The centrosome protein AKNA regulates neurogenesis via microtubule organization. *Nature.* 567:113–117. https://doi.org/10.1038/s41586-019-0962-4

Cunha-Ferreira, I., A. Chazeau, R.R. Buijs, R. Stucchi, L. Will, X. Pan, Y. Adolfs, C. van der Meer, J.C. Wolthuis, O.I. Kahn, et al. 2018. The HAUS Complex Is a Key Regulator of Non-centrosomal Microtubule Organization during Neuronal Development. *Cell Rep.* 24:791–800. https://doi.org/10.1016/j.celrep.2018.06.093

Efimov, A., A. Kharitonov, N. Efimova, J. Loncarek, P.M. Miller, N. Andreyeva, P. Gleeson, N. Galjart, A.R.R. Maia, I.X. McLeod, et al. 2007. Asymmetric CLASP-dependent nucleation of noncentrosomal microtubules at the trans-Golgi network. *Dev. Cell.* 12:917–930. https://doi.org/10.1016/j.devcel.2007.04.002

Feng, C., P. Thyagarajan, M. Shorey, D.Y. Seebold, A.T. Weiner, R.M. Albertson, K.S. Rao, A. Sagasti, D.J. Goetschius, and M.M. Rolls. 2019. Patronin-mediated minus end growth is required for dendritic microtubule polarity. *J. Cell Biol.* 218(7):2309–2328. https://doi.org/10.1083/jcb.201810155

Fernández, V., C. Llinares-Benadero, and V. Borrell. 2016. Cerebral cortex expansion and folding: what have we learned? *EMBO J.* 35:1021–1044. https://doi.org/10.15252/embj.201593701

Fietz, S.A., I. Kelava, J. Vogt, M. Wilsch-Bräuninger, D. Stenzel, J.L. Fish, D. Corbeil, A. Riehn, W. Distler, R. Nitsch, and W.B. Huttner. 2010. OSVZ progenitors of human and ferret neocortex are epithelial-like and expand by integrin signaling. *Nat. Neurosci.* 13:690–699. https://doi.org/10.1038/nn.2553

Guedes-Dias, P., J.J. Nirschl, N. Abreu, M.K. Tokito, C. Janke, M.M. Magiera, and E.L.F. Holzbaur. 2019. Kinesin-3 Responds to Local Microtubule Dynamics to Target Synaptic Cargo Delivery to the Presynapse. *Curr. Biol.* 29:268–282.e8. https://doi.org/10.1016/j.cub.2018.11.065

Hansen, D.V., J.H. Lui, P.R.L. Parker, and A.R. Kriegstein. 2010. Neurogenic radial glia in the outer subventricular zone of human neocortex. *Nature.* 464:554–561. https://doi.org/10.1038/nature08845

Horton, A.C., and M.D. Ehlers. 2003. Dual modes of endoplasmic reticulum-to-Golgi transport in dendrites revealed by live-cell imaging. *J. Neurosci.* 23:6188–6199. https://doi.org/10.1523/JNEUROSCI.23-15-06188.2003

Horton, A.C., B. Rácz, E.E. Monson, A.L. Lin, R.J. Weinberg, and M.D. Ehlers. 2005. Polarized secretory trafficking directs cargo for asymmetric dendrite growth and morphogenesis. *Neuron.* 48:757–771. https://doi.org/10.1016/j.neuron.2005.11.005

Hu, D.J.-K., A.D. Baffet, T. Nayak, A. Akhmanova, V. Doye, and R.B. Vallee. 2013. Dynein Recruitment to Nuclear Pores Activates Apical Nuclear Migration and Mitotic Entry in Brain Progenitor Cells. *Cell.* 154(6): 1300–1313. https://doi.org/10.1016/j.cell.2013.08.024

Hu, W.F., O. Pomp, T. Ben-Omran, A. Kodani, K. Henke, G.H. Mochida, T.W. Yu, M.B. Woodworth, C. Bonnard, G.S. Raj, et al. 2014. Katanin p80 regulates human cortical development by limiting centriole and cilia number. *Neuron.* 84:1240–1257. https://doi.org/10.1016/j.neuron.2014.12.017

Jayaraman, D., B.-I. Bae, and C.A. Walsh. 2018. The Genetics of Primary Microcephaly. *Annu. Rev. Genomics Hum. Genet.* 19:177–200. https://doi.org/10.1146/annurev-genom-083117-021441

Jiang, K., S. Hua, R. Mohan, I. Grigoriev, K.W. Yau, Q. Liu, E.A. Katrukha, A.F.M. Altelaar, A.J.R. Heck, C.C. Hoogenraad, and A. Akhmanova. 2014. Microtubule minus-end stabilization by polymerization-driven CAMSAP deposition. *Dev. Cell.* 28:295–309. https://doi.org/10.1016/j.devcel.2014.01.001

Kapitein, L.C., M.A. Schlager, M. Kuijpers, P.S. Wulf, M. van Spronsen, F.C. MacKintosh, and C.C. Hoogenraad. 2010. Mixed microtubules steer dynein-driven cargo transport into dendrites. *Curr. Biol.* 20:290–299. https://doi.org/10.1016/j.cub.2009.12.052

Kriegstein, A., and A. Alvarez-Buylla. 2009. The glial nature of embryonic and adult neural stem cells. *Annu. Rev. Neurosci.* 32:149–184. https://doi.org/10.1146/annurev.neuro.051508.135600

Lui, J.H., D.V. Hansen, and A.R. Kriegstein. 2011. Development and evolution of the human neocortex. *Cell.* 146:18–36. https://doi.org/10.1016/j.cell.2011.06.030

Nakagawa, N., C. Plestant, K. Yabuno-Nakagawa, J. Li, J. Lee, C.-W. Huang, A. Lee, O. Krupa, A. Adhikari, S. Thompson, et al. 2019. Memo1-Mediated Tiling of Radial Glial Cells Facilitates Cerebral Cortical Development. *Neuron.* 103:836–852.e5. https://doi.org/10.1016/j.neuron.2019.05.049

Noctor, S.C., V. Martínez-Cerdeño, L. Ivic, and A.R. Kriegstein. 2004. Cortical neurons arise in symmetric and asymmetric division zones and migrate through specific phases. *Nat. Neurosci.* 7:136–144. https://doi.org/10.1038/nn1172

Noctor, S.C., A.C. Flint, T.A. Weissman, R.S. Dammerman, and A.R. Kriegstein. 2001. Neurons derived from radial glial cells establish radial units in neocortex. *Nature.* 409(6821):714–720. https://doi.org/10.1038/35055553

Ori-McKenney, K.M., L.Y. Jan, and Y.-N. Jan. 2012. Golgi outposts shape dendrite morphology by functioning as sites of acentrosomal microtubule nucleation in neurons. *Neuron.* 76:921–930. https://doi.org/10.1016/j.neuron.2012.10.008

Paridaen, J.T., and W.B. Huttner. 2014. Neurogenesis during development of the vertebrate central nervous system. *EMBO Rep.* 15:351–364. https://doi.org/10.1002/embr.201438447

Pilaz, L.-J., A.L. Lennox, J.P. Rouanet, and D.L. Silver. 2016. Dynamic mRNA Transport and Local Translation in Radial Glial Progenitors of the Developing Brain. *Curr. Biol.* 26:3383–3392. https://doi.org/10.1016/j.cub.2016.10.040

Pinson, A., T. Namba, and W.B. Huttner. 2019. Malformations of Human Neocortex in Development - Their Progenitor Cell Basis and Experimental Model Systems. *Front. Cell. Neurosci.* 13:305. https://doi.org/10.3389/fncel.2019.00305

Poirier, K., N. Lebrun, L. Broix, G. Tian, Y. Saillour, C. Boscheron, E. Parrini, S. Valence, B.S. Pierre, M. Oger, et al. 2013. Mutations in TUBG1, DYNC1H1, KIF5C and KIF2A cause malformations of cortical development and microcephaly. *Nat. Genet.* 45:639–647. https://doi.org/10.1038/ng.2613

Qu, X., A. Kumar, H. Blockus, C. Waites, and F. Bartolini. 2019. Activity-Dependent Nucleation of Dynamic Microtubules at Presynaptic Boutons Controls Neurotransmission. *Curr. Biol.* 29:4231–4240.e5. https://doi.org/10.1016/j.cub.2019.10.049

Reillo, I., C. de Juan Romero, M.Á. García-Cabezas, and V. Borrell. 2011. A role for intermediate radial glia in the tangential expansion of the mammalian cerebral cortex. *Cereb. Cortex.* 21:1674–1694. https://doi.org/10.1093/cercor/bhq238

Reiner, O., R. Carrozzo, Y. Shen, M. Wehnert, F. Faustinella, W.B. Dobyns, C.T. Caskey, and D.H. Ledbetter. 1993. Isolation of a Miller-Dieker lissencephaly gene containing G protein beta-subunit-like repeats. *Nature.* 364:717–721. https://doi.org/10.1038/364717a0

Sánchez-Huertas, C., F. Freixo, R. Viais, C. Lacasa, E. Soriano, and J. Lüders. 2016. Non-centrosomal nucleation mediated by augmin organizes microtubules in post-mitotic neurons and controls axonal microtubule polarity. *Nat. Commun.* 7:12187. https://doi.org/10.1038/ncomms12187

Shitamukai, A., D. Konno, and F. Matsuzaki. 2011. Oblique radial glial divisions in the developing mouse neocortex induce self-renewing progenitors outside the germinal zone that resemble primate outer subventricular zone progenitors. *J. Neurosci.* 31:3683–3695. https://doi.org/10.1523/JNEUROSCI.4773-10.2011

Tan, X., and S.-H. Shi. 2013. Neocortical neurogenesis and neuronal migration. *Wiley Interdiscip. Rev. Dev. Biol.* 2:443–459. https://doi.org/10.1002/wdev.88

Tas, R.P., A. Chazeau, B.M.C. Cloin, M.L.A. Lambers, C.C. Hoogenraad, and L.C. Kapitein. 2017. Differentiation between Oppositely Oriented Microtubules Controls Polarized Neuronal Transport. *Neuron.* 96: 1264–1271.e5. https://doi.org/10.1016/j.neuron.2017.11.018

Taverna, E., M. Götz, and W.B. Huttner. 2014. The cell biology of neurogenesis: toward an understanding of the development and evolution of the neocortex. *Annu. Rev. Cell Dev. Biol.* 30:465–502. https://doi.org/10.1146/annurev-cellbio-101011-155801

Taverna, E., F. Mora-Bermúdez, P.J. Strzyz, M. Florio, J. Icha, C. Haffner, C. Norden, M. Wilsch-Bräuninger, and W.B. Huttner. 2016. Non-canonical features of the Golgi apparatus in bipolar epithelial neural stem cells. *Sci. Rep.* 6:21206. https://doi.org/10.1038/srep21206

Telley, L., G. Agirman, J. Prados, N. Amberg, S. Fièvre, P. Oberst, G. Bartolini, I. Vitali, C. Cadilhac, S. Hippenmeyer, et al. 2019. Temporal patterning of apical progenitors and their daughter neurons in the developing neocortex. *Science.* 364:eaav2522–9. https://doi.org/10.1126/science.aav2522

Tsai, J.-W., K.H. Bremner, and R.B. Vallee. 2007. Dual subcellular roles for LIS1 and dynein in radial neuronal migration in live brain tissue. *Nat. Neurosci.* 10:970–979. https://doi.org/10.1038/nn1934

Tsai, J.-W., W.-N. Lian, S. Kemal, A.R. Kriegstein, and R.B. Vallee. 2010. Kinesin 3 and cytoplasmic dynein mediate interkinetic nuclear migration in neural stem cells. *Nat. Neurosci.* 13:1463–1471. https://doi.org/10.1038/nn.2665

Tsunekawa, Y., J.M. Britto, M. Takahashi, F. Polleux, S.-S. Tan, and N. Osumi. 2012. Cyclin D2 in the basal process of neural progenitors is linked to non-equivalent cell fates. *EMBO J.* 31:1879–1892. https://doi.org/10.1038/emboj.2012.43

Wang, Y., M. Rui, Q. Tang, S. Bu, and F. Yu. 2019. Patronin governs minus-end-out orientation of dendritic microtubules to promote dendrite pruning in Drosophila. *eLife.* 8:e39964. https://doi.org/10.7554/eLife.39964

Wu, J., C. de Heus, Q. Liu, B.P. Bouchet, I. Noordstra, K. Jiang, S. Hua, M. Martin, C. Yang, I. Grigoriev, et al. 2016. Molecular Pathway of Microtubule Organization at the Golgi Apparatus. *Dev. Cell.* 39:44–60. https://doi.org/10.1016/j.devcel.2016.08.009

Yau, K.W., S.F.B. van Beuningen, I. Cunha-Ferreira, B.M.C. Cloin, E.Y. van Battum, L. Will, P. Schätzle, R.P. Tas, J. van Krugten, E.A. Katrukha, et al. 2014. Microtubule Minus-End Binding Protein CAMSAP2 Controls Axon Specification and Dendrite Development. *Neuron.* 82(5):1058–1073. https://doi.org/10.1016/j.neuron.2014.04.019

Yau, K.W., P. Schätzle, E. Tortosa, S. Pagès, A. Holtmaat, L.C. Kapitein, and C.C. Hoogenraad. 2016. Dendrites In Vitro and In Vivo Contain Microtubules of Opposite Polarity and Axon Formation Correlates with Uniform Plus-End-Out Microtubule Orientation. *J. Neurosci.* 36:1071–1085. https://doi.org/10.1523/JNEUROSCI.2430-15.2016

Ye, B., Y. Zhang, W. Song, S.H. Younger, L.Y. Jan, and Y.-N. Jan. 2007. Growing dendrites and axons differ in their reliance on the secretory pathway. *Cell.* 130:717–729. https://doi.org/10.1016/j.cell.2007.06.032

Yokota, Y., W.-Y. Kim, Y. Chen, X. Wang, A. Stanco, Y. Komuro, W. Snider, and E.S. Anton. 2009. The adenomatous polyposis coli protein is an essential regulator of radial glial polarity and construction of the cerebral cortex. *Neuron.* 61:42–56. https://doi.org/10.1016/j.neuron.2008.10.053

Yokota, Y., T.-Y. Eom, A. Stanco, W.-Y. Kim, S. Rao, W.D. Snider, and E.S. Anton. 2010. Cdc42 and Gsk3 modulate the dynamics of radial glial growth, inter-radial glial interactions and polarity in the developing cerebral cortex. *Development.* 137:4101–4110. https://doi.org/10.1242/dev.048637

## Supplemental material

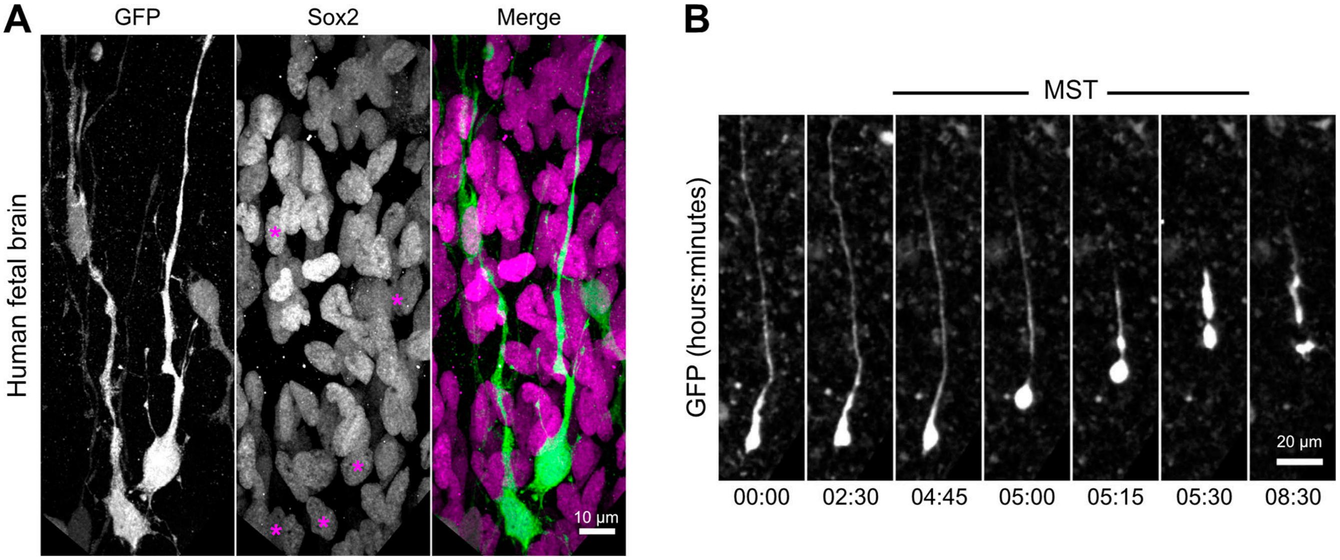

Figure S1. **Validation of bRG cell fate in human fetal tissue. Related to Fig. 3. (A)** GFP-electroporated bRG cells positive for RG marker Sox2 in human fetal brain tissue. Purple asterisks indicate electroporated cell soma. **(B)** Live imaging of a human fetal bRG cell undergoing MST before cell division.

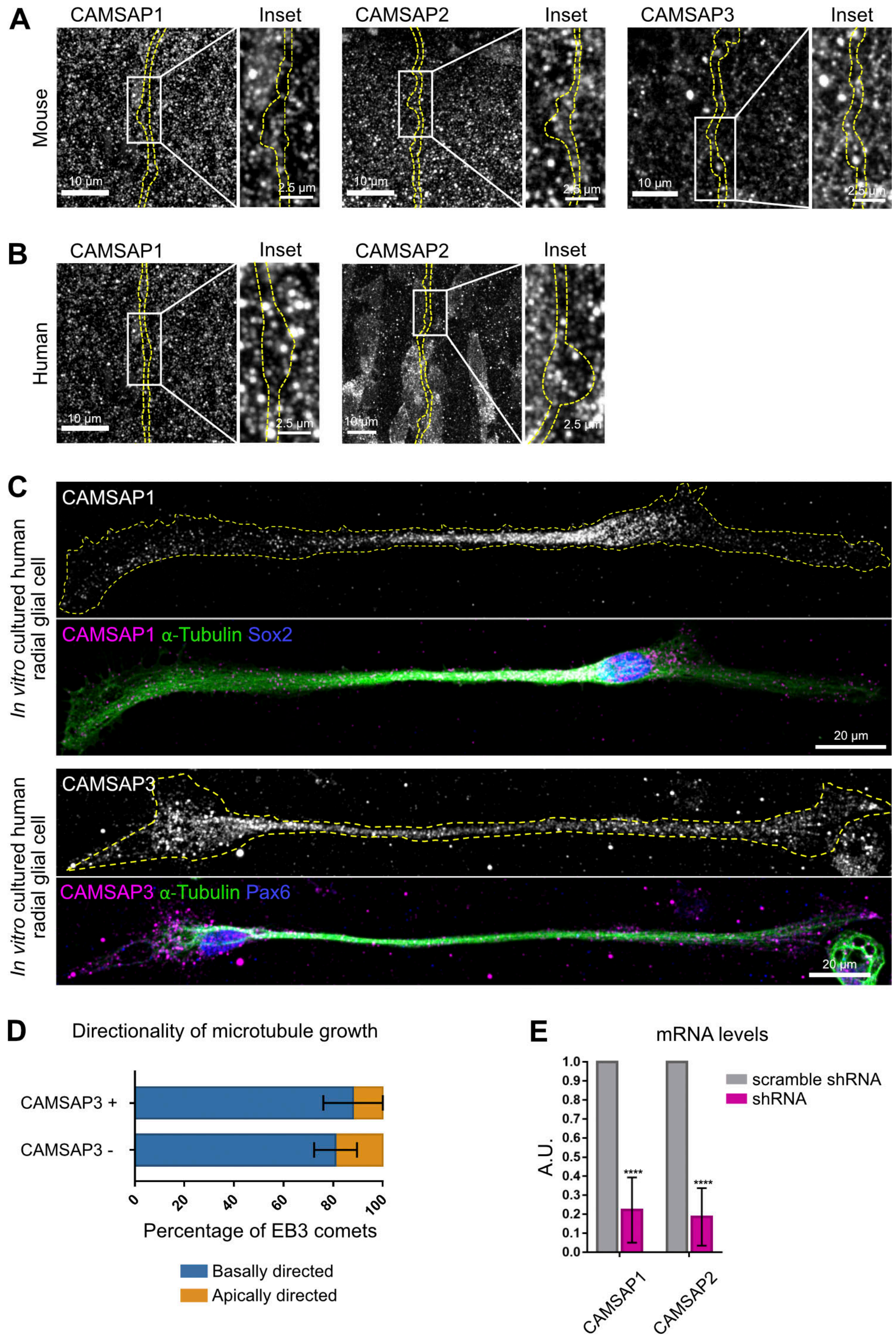

Figure S2. **CAMSAP 1, 2, and 3 endogenous localization and KD validation.** Related to Fig. 4 and Fig. 5. **(A)** Immunostaining for CAMSAP1, CAMSAP2, and CAMSAP3 in GFP-electroporated mouse cortical tissue. **(B)** Immunostaining for CAMSAP1 and CAMSAP2 in GFP-electroporated human cortical tissue. **(C)** Immunostaining for CAMSAP1 and CAMSAP3, together with Sox2 and α-tubulin, in human RG cells cultured in vitro. **(D)** Directionality of microtubule growth depending on whether EB3 comet emanates within or away from CAMSAP3-positive foci ($n$ = 252 comets from 15 cells). **(E)** Quantitative PCR measurement of CAMSAP 1 and 2 mRNA levels following KD in Neuro2A cells. ****, P <0.0001. Error bars indicate SD. A.U., arbitrary units.

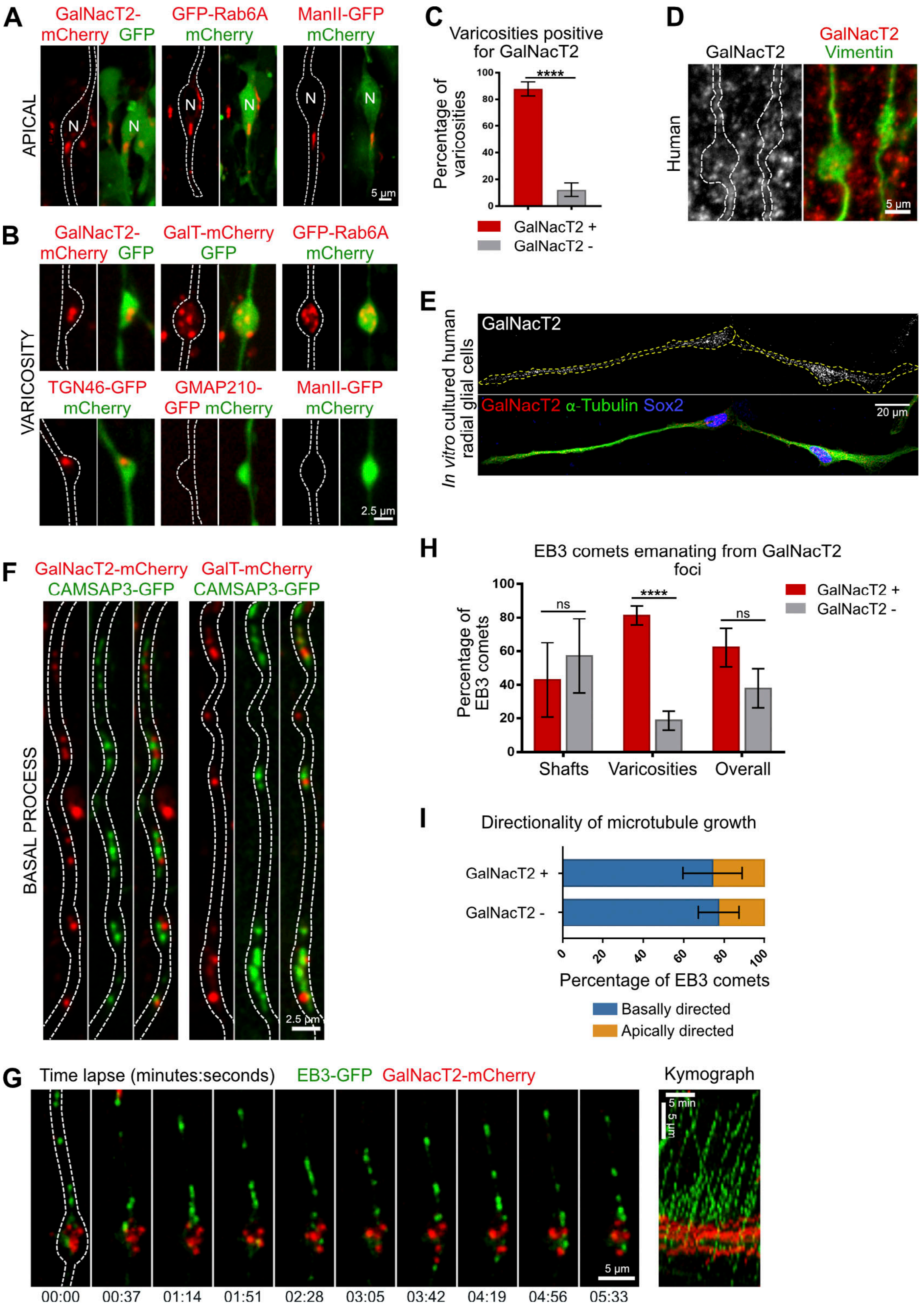

Figure S3. **A Golgi-related compartment localizes to microtubule minus ends in basal process varicosities. (A)** Localization of GalNacT2-mCherry, GFP-Rab6A, and ManII-GFP in aRG apical process. N, nucleus. **(B)** Localization of GalNacT2-mCherry, GalT-mCherry, and GFP-Rab6A, TGN46-GFP, GMAP210-GFP, and ManII-GFP in aRG basal process varicosities. **(C)** Quantification of the percentage of basal process varicosities positive for GalNacT2 (*n* = 70 varicosities in 13 cells). **(D)** Immunostaining for GalNacT2 in Vimentin-stained cortical tissue. **(E)** Immunostaining for GalNacT2, together with Sox2 and α-tubulin, in human RG cells cultured in vitro. **(F)** Co-expression of GalNacT2-mCherry and GalT-mCherry with CAMSAP3-GFP in basal process of mouse aRG cells. **(G)** Live imaging of EB3-GFP and GalNacT2-mCherry in mouse aRG cell basal process and corresponding kymograph. **(H)** Quantification of the percentage of EB3 comets emanating from GalNacT2-positive foci throughout the basal process, in shafts and in varicosities (*n* = 333 comets from 28 cells). **(I)** Directionality of microtubule growth depending on whether EB3 comet emanates within or away from GalNacT2-positive foci (*n* = 274 comets from 28 cells). ****, $P < 0.0001$ by Mann-Whitney tests. All experiments were performed in at least three independent mice or two independent human samples. Error bars indicate SD.

Video 1. **EB3-GFP dynamics in apical process of mouse aRG cells.** EB3-GFP was electroporated at E13.5, and brain was sectioned and imaged at E14.5. The majority of microtubule plus ends grow basally. Scale bar: 5 µm. 15 fps.

Video 2. **EB3-GFP dynamics in basal process of mouse aRG cells.** EB3-GFP was electroporated at E13.5, and brain was sectioned and imaged at E14.5. Microtubules can be observed to grow basally and apically. Scale bar: 5 µm. 15 fps.

Video 3. **EB3-GFP dynamics in the medial part of the basal process of mouse aRG cells.** EB3-GFP was electroporated at E13.5, and brain was sectioned and imaged along the apico-basal axis at E14.5. Microtubule polarity is similar throughout most of the basal process, except at the apical-most region where most microtubules grow basally. Scale bar: 5 µm. 10 fps.

Video 4. **Long-term dynamics of basal process swelling.** GFP was electroporated at E13.5, and brain was sectioned and imaged at E14.5. Cells are highly dynamic, undergoing interkinetic nuclear migration. The majority of swellings are stable throughout a 22-h movie. Scale bar: 100 µm. 25 fps.

Video 5. **Long-term dynamics of basal process swelling (inset).** GFP was electroporated at E13.5, and brain was sectioned and imaged at E14.5. The majority of swellings are stable throughout a 22-h movie. Scale bar: 10 µm. 10 fps.

Video 6. **EB3-GFP dynamics in basal process swelling of mouse aRG cells.** EB3-GFP was electroporated at E13.5, and brain was sectioned and imaged at E14.5. Intense EB3 comet formation is observed within basal process swellings. Scale bar: 5 µm. 15 fps.

Video 7. **Human bRG cell undergoing MST.** Gestational week 18 human fetal brain was electroporated with GFP, sectioned, cultured for 24 h, and imaged. The soma of bRG cell undergoes rapid movement before cell division. Scale bar: 20 µm. 25 fps.

Video 8. **EB3-GFP dynamics in basal process swelling of human bRG cells.** Gestational week 18 human fetal brain was electroporated with EB3-GFP, sectioned, cultured for 48 h, and imaged. Intense EB3 comet formation is observed within basal process swellings. Scale bar: 2.5 µm. 10 fps.

Video 9. **EB3-mCherry comets emanating from CAMSAP3-GFP foci.** EB3-RFP and CAMSAP3-GFP were electroporated at E13.5, and brain was sectioned and imaged at E14.5. The majority of novel EB3 comets emanate from CAMSAP3 foci. Scale bar: 5 µm. 15 fps.

Video 10. **EB3-mCherry comets emanating from GFP-CAMSAP1 foci.** EB3-RFP and CAMSAP3-GFP were electroporated at E13.5, and brain was sectioned and imaged at E14.5. An EB3 comet can be seen emanating from a CAMSAP1 focus. Scale bar: 2.5 µm. 10 fps.

Video 11. **EB3-GFP dynamics in a varicosity of a scramble shRNA-expressing RG cell.** EB3-GFP and scramble shRNA plasmids were electroporated at E13.5, and brain was sectioned and imaged at E15.5. Scale bar: 2.5 µm. 10 fps.

Video 12. **EB3-GFP dynamics in a varicosity of a CAMSAP1 shRNA-expressing RG cell.** EB3-GFP and CAMSAP1 shRNA plasmids were electroporated at E13.5, and brain was sectioned and imaged at E15.5. Scale bar: 2.5 µm. 10 fps.

Video 13. **EB3-GFP dynamics in a varicosity of a CAMSAP2 shRNA-expressing RG cell.** EB3-GFP and CAMSAP2 shRNA plasmids were electroporated at E13.5, and brain was sectioned and imaged at E15.5. Scale bar: 2.5 µm. 10 fps.

Video 14. **EB3-GFP comets emanating from GalNacT2-RFP foci.** EB3-GFP and GalNacT2-RFP were electroporated at E13.5, and brain was sectioned and imaged at E14.5. The majority of novel EB3 comets emanate from GalNacT2 foci. Scale bar: 5 µm. 15 fps.